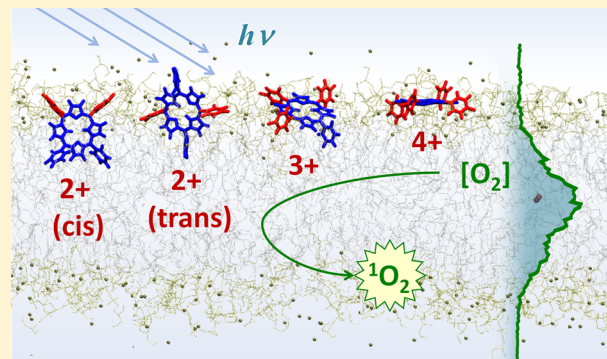


Photodynamic Efficiency of Cationic *meso*-Porphyrs at Lipid Bilayers: Insights from Molecular Dynamics Simulations

Rodrigo M. Cordeiro,^{*†} Ronei Miotto,[†] and Maurício S. Baptista[‡][†]Centro de Ciências Naturais e Humanas, Universidade Federal do ABC, Rua Santa Adélia 166, CEP 09210-170, Santo André (SP), Brazil[‡]Departamento de Bioquímica, Instituto de Química, Universidade de São Paulo, Av. Prof. Lineu Prestes 748, CEP 05508-900, São Paulo (SP), Brazil

Supporting Information

ABSTRACT: Porphyrin derivatives have applications as photoactive drugs in photodynamic therapy. However, little is known about their interactions with phospholipid membranes at the molecular level. We employed molecular dynamics simulations to model the binding between a series of cationic *meso*-(*N*-methyl-4-pyridinium)phenylporphyrins and anionic phosphatidylglycerol lipid bilayers. This was done in the presence of molecular oxygen within the membrane. The ability of various porphyrins to cause photodamage was quantified in terms of their immersion depth and degree of exposition to a higher oxygen concentration inside the membrane. Simulations showed that the photodynamic efficiency could be improved as the number of hydrophobic phenyl substituents attached to the porphyrinic ring increased. In the specific case of porphyrins containing two hydrophobic and two charged substituents, the *cis* isomer was significantly more efficient than the *trans*. These results correlate well with previous experimental observations. They highlight the importance of both the total charge and amphiphilicity of the photosensitizer for its performance in photodynamic therapy.



1. INTRODUCTION

In the past years, photodynamic therapy (PDT) has emerged as a powerful strategy for the treatment of neoplasm-related diseases.¹ It is increasingly becoming part of clinical practices in oncology. Other applications have also appeared, including the treatment of bacterial infections^{2–4} and even tropical diseases like malaria and leishmaniasis.^{5,6} In particular, the antimicrobial application of PDT is a promising area due to the continuously growing resistance of pathogens to commonly used antibiotics.

With respect to its mechanism of action, PDT is based on the combination between a photoactive drug (photosensitizer), a light source, and molecular oxygen. The absorption of light by the photosensitizer leads to the formation of excited states, followed either by direct electron transfer to biological substrates (type I mechanism) or by energy transfer to oxygen present in the medium (type II mechanism). Type II reactions result in the formation of the short-lived and highly reactive singlet oxygen (${}^1\text{O}_2$). Its spatial range of action is limited to approximately 45 nm in cellular media,⁷ but its reactivity toward monounsaturated alkyl chains is 4 orders of magnitude higher when compared to that of common oxygen.⁸ Consequently, ${}^1\text{O}_2$ can react almost indiscriminately with all pieces of the cell machinery, including phospholipid membranes, and is considered as the main cytotoxic agent in PDT.

Considerable effort has been expended in the development of photosensitizers for efficient *in situ* generation of ${}^1\text{O}_2$. A few

porphyrin derivatives have already been approved for clinical use.^{9–11} A myriad of aspects must be considered simultaneously, including pharmacokinetic issues, stability, safety, and price. From the chemical point of view, attention is given to the drug–membrane binding affinity. It is desirable that photosensitizers have an amphiphilic structure: while the hydrophilic part ensures water solubility, allowing for intravenous administration, the hydrophobic part improves the drug–membrane affinity.¹¹ This trend is supported by a number of experimental results^{12–15} with emphasis on the investigations of Engelmann et al.^{16,17} for a series of cationic *meso*-(*N*-methyl-3-pyridinium)phenylporphyrins. However, it is noteworthy that the large differences observed in the photodynamic efficiency cannot be solely ascribed to differences in the intrinsic efficiency or in the drug–membrane binding affinity of different porphyrins. Additional issues were proposed as being important, such as the relative positions and orientations of different photosensitizers at the membrane–water interface and consequently their accessibility to the hydrophobic membrane interior, where the oxygen concentration is higher than in the aqueous medium.^{17–19} However, it is difficult to measure all these aspects directly in experiments.

Received: August 16, 2012

Revised: September 26, 2012

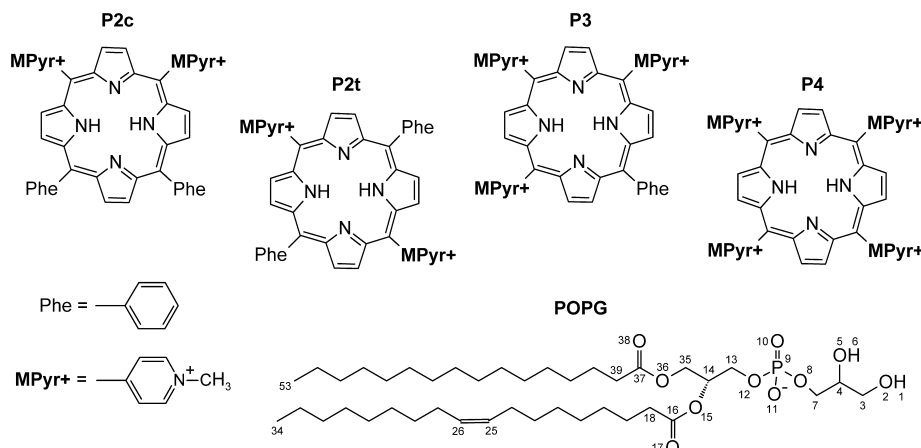


Figure 1. Chemical structures of several *meso*-(*N*-methyl-4-pyridinium)phenylporphyrins and of the POPG lipid. Atoms of the lipid chain are numbered for better distinction of the phosphate group (atoms O8, P9, O10, O11, O12), the carboxylester groups (O15, C16, O17, O36, C37, O38), and the hydrocarbon chain unsaturation (C25, C26).

Molecular modeling techniques are well-suited for this task. They are able to provide information on structure and interactions at the molecular level for chemically realistic systems. There are several works in the literature dealing with the computational modeling of photosensitizers at phospholipid membranes.^{20–25} However, there is a lack of systematic studies in which a link with photodynamic efficiency is established in terms of experimentally verifiable structure–property relations. Furthermore, biological membranes targeted by PDT often bear a substantial amount of negative charge, and this aspect has not always been considered. In the present work, we focus attention on membrane models made of anionic phosphatidylglycerols (PGs). Typically, the amount of PGs in bacterial membranes is ca. 25%²⁶ but reaches up to 90% in certain human pathogens like *Staphylococcus aureus*.²⁷ In turn, the inner mitochondrial membrane contains ca. 14% of cardiolipin,²⁸ a divalent phospholipid in which two phosphatidyl moieties are linked together through a central glycerol group (the structure is equivalent to a PG dimer).²⁹ In erythrocytes, PGs constitute only ca. 2% of all phospholipids,³⁰ but the anionic character of the membrane is preserved by a significant amount of phosphatidylserine and other anionic lipids.³¹

In the present work, we employed molecular dynamics (MD) simulations^{32,33} to model the binding between a series of cationic *meso*-(*N*-methyl-4-pyridinium)phenylporphyrins and anionic phosphatidylglycerol (PG) lipid bilayers. Our results provide a molecular view of some of the structure–property relations that are relevant for the photodynamic efficiency of porphyrin photosensitizers at the membrane–water interface. These results are compared to experimental data and include the estimation of the photodynamic efficiency of the considered drugs. We believe that the concepts learned and the calculation protocols here presented will help in the chemical design of novel drugs for PDT.

2. SIMULATION METHODS

2.1. Membrane Model. Anionic lipid bilayers made of 1-palmitoyl-2-oleoyl-*sn*-glycero-3-phosphoglycerol (POPG) were represented using the force field developed by Kukol.³⁴ The interaction parameters are based on the GROMOS 53A6 force field,³⁵ in which aliphatic carbon atoms and their adjacent hydrogens are treated as united atoms. Figure 1 shows the

structure of POPG. To simulate fully hydrated lipid bilayers, the SPC model³⁶ was used for water, and Na⁺ ions were added up to keep electroneutrality. The oxygen molecule dissolved in the membrane was described with parameters taken from the literature.³⁷

Kukol's lipid model yields an area per lipid of $70.0 \pm 0.7 \text{ \AA}^2$, close to a recently reported value of $66.0 \pm 1.3 \text{ \AA}^2$, which was determined by means of a model-based analysis of neutron and X-ray scattering data.³⁸ However, the existence of a few inconsistencies in Kukol's force field for POPG have been reported,³⁹ as for instance its inability to accurately predict the order degree of lipid hydrocarbon tails. An in-depth analysis of these aspects is outside the scope of the present work.

2.2. Photosensitizer Models. A series of substituted porphyrins were simulated, differing with respect to both the relative number and spatial distribution of charged *N*-methyl-4-pyridinium (MPyr+) groups and apolar phenyl (Phe) groups attached to the central porphyrin ring. Figure 1 shows the structures of the simulated compounds, which were: *meso*-*di-cis*(*N*-methyl-4-pyridyl)diphenylporphyrin chloride (P2c); *meso*-*di-trans*(*N*-methyl-4-pyridyl)diphenylporphyrin chloride (P2t); *meso*-*tri*(*N*-methyl-4-pyridyl)monophenylporphyrin chloride (P3); and *meso*-*tetra*(*N*-methyl-4-pyridyl)porphyrin chloride (P4). A comprehensive documentation of the force field parameters used for these compounds can be found in Figure S1 in the Supporting Information. All van der Waals and bonded interaction parameters were pieced together from the GROMOS 53A6 library³⁵ by analogy with existing structures. The missing torsions at the links between the porphyrin ring and the substituents were taken from the density functional calculations of Barone et al.⁴⁰ Partial charges were adapted from the work of Karachevtsev et al.⁴¹ To evaluate the sensitivity of the results to the specific choice of the photosensitizer force field parameters, several other sets of atomic partial charges were taken from the literature^{40,42–45} and used to describe the photosensitizers. These charge sets, which were derived according to different protocols, were compared in terms of their influence upon the immersion depth and orientation of P2c at the membrane–water interface.

2.3. Simulation Details. Molecular dynamics simulations were performed with a single precision version of the GROMACS 4.5.1 simulation package.^{46,47} A leapfrog integrator^{32,33} was used with a time step of 2 fs. Electrostatic

interactions were treated by the particle mesh Ewald (PME) method^{48,49} with a real space cutoff of 0.9 nm, a Fourier mesh spacing of 0.12 nm, and a fourth-order interpolation. Lennard-Jones interactions were truncated using a twin-range cutoff at 0.9 and 1.4 nm. A neighbor list with a 0.9 nm cutoff was updated every 10 steps. Long-range dispersion corrections were applied for both energy and pressure. Center of mass motion was removed every 10 steps for both the bilayer and the aqueous phase independently. All bonds were constrained to their equilibrium values using the LINCS algorithm,^{50,51} except for bonds within water molecules, which were constrained using the SETTLE algorithm.⁵²

Initial coordinates were taken from a pre-equilibrated membrane patch provided by Kukol.³⁴ The membrane patch contained 128 POPG lipids and was chirally neutral with respect to the glycerol headgroups, with equal numbers of *D*-POPG and *L*-POPG. The membrane was at a fully hydrated state and contained 128 Na⁺ counterions to keep electro-neutrality. The system was expanded in the direction of the bilayer normal, and the photosensitizer was placed ca. 3 nm away from the membrane surface. The system was filled with water, and enough Cl⁻ counterions were added up to neutralize the charge of the photosensitizer. A single oxygen molecule was added to the aqueous phase. This reflects the low solubility of oxygen in water, which is in the range of parts per million.⁵³ The assembled systems had lateral dimensions of ca. 6.6 nm parallel to the membrane surface (*xy* plane) and ca. 10 nm along the bilayer normal (*z* axis). Periodic boundary conditions were applied in all Cartesian directions.

Simulations started with a pre-equilibration phase, during which the position of the porphyrin ring was kept restrained. This phase consisted of an energy minimization, followed by 500 ps of thermal equilibration in the isothermal–isovolumetric (NVT) ensemble, followed in turn by a 5 ns run in the isothermal–isobaric (NPT) ensemble for relaxation of the pressure and the ionic cloud configuration. After this pre-equilibration, a longer NPT equilibration run was performed, in which the photosensitizer was free to move and to interact with the lipid bilayer. Temperature was set to 310 K, well above the gel to liquid-crystalline transition temperature of POPG.^{34,54} Temperature control was accomplished by a Nosé-Hoover thermostat^{55,56} with a coupling time constant of 0.5 ps. Two separate coupling groups were defined: one containing all water molecules and ions and the other containing the lipids, the photosensitizer, and the oxygen molecule. Pressure was kept at 1 bar by a Parrinello–Rahman barostat^{57,58} with a coupling time constant of 2.0 ps and a compressibility of 4.5×10^{-5} bar⁻¹. A semianisotropic coupling scheme was applied to allow for independent variation of the system length in the *z* direction and the membrane area at the *xy* plane. Trajectories in the xtc format were recorded at regular intervals of 20 ps. After 200–300 ns of equilibration, trajectories were extended for 100 ns for sampling of average data. Additional simulations of some of the photosensitizers in cubic water boxes (lateral dimensions of ca. 5 nm) were performed to study their hydration structure. These simulations were based on similar technical details and included an equilibration period of more than 20 ns, followed by data acquisition for 100 ns. The total computational effort exceeded 2 μ s of simulation time.

2.4. Data Analysis. The drug–membrane binding process was followed in time by recording both the position and the orientation of the different photosensitizers with respect to the bilayer. Average values and standard deviations were calculated

over the last 100 ns of simulation. Density distributions of the membrane building blocks and the photosensitizers were calculated along the *z* axis. The degree of overlap between the distributions of photosensitizers and molecular oxygen was taken as an indicator of the expected $^1\text{O}_2$ generation efficiency. Complete information on the spatial patterns of lipid functional groups around the photosensitizers was obtained by means of three-dimensional spatial distribution functions (SDFs). The SDFs were computed using the g_spatial tool implemented in GROMACS. Successive trajectory frames were translated and rotated so as to minimize the root-mean-square deviation between the positions of atoms at the central porphyrin ring. With this new frame of reference, three-dimensional density distributions around the photosensitizers were built by dividing the space in cubic cells of 0.5 Å and calculating their average occupancy. Simulation snapshots and SDF isosurfaces were rendered graphically using the software VMD.⁵⁹ The photosensitizer lateral mobility was assessed by following in time its center of mass trajectory with respect to the membrane in the last 100 ns of simulation (any lateral drift of bilayer leaflets with respect to each other was neglected). In nuclear magnetic resonance experiments, the ordering of lipid hydrocarbon tails is characterized by the so-called “deuterium order parameter”. In simulations, the order parameter of individual C–H bonds was determined with respect to the bilayer normal using the g_order tool. The order parameter $S_{z,i}$ associated to a carbon atom at position *i* along the chain is given by⁶⁰

$$S_{z,i} = \frac{1}{2} \langle 3 \cos^2 \theta_{z,i} - 1 \rangle \quad (1)$$

where $\theta_{z,i}$ is the angle formed between a C–H bond of the *i*th carbon and the *z* axis. The angular brackets indicate an ensemble average. Since the GROMOS force field uses a united-atom representation of hydrocarbon chains, hydrogens attached to a given carbon atom were constructed based on the position of the adjacent carbons along the chain, to preserve tetrahedral geometry.

3. RESULTS AND DISCUSSION

3.1. Structure and Hydration of the Photosensitizers.

The main structural features of cationic meso-(*N*-methyl-4-pyridinium)phenylporphyrins were well represented by the model. The conformation of the central porphyrin ring fluctuated around a planar geometry with small out-of-plane distortions of the substituents, as shown in Figure 2. The dihedral angle between the aromatic substituents and the central porphyrin ring was ca. 60°, in line with another theoretical work.⁴⁰ The torsional potential of the substituents had energy barriers at 0° and 90°, both with a periodicity of 180°. At 310 K and within simulation time, only the second barrier could be overcome, meaning that the substituents had restricted rotation ability. The SDF of water molecules revealed a moderate hydration of the central porphyrin ring, especially of the nitrogen atoms, in agreement with the trends reported by Guizado et al.^{61–63} Hydration was more pronounced for the Mpyr+ as compared to the Phe groups. In fact, experimental measurements of *n*-butanol/water partition coefficients (see Table 1) demonstrate that the affinity of the different photosensitizers for water is improved as the number of strongly hydrated Mpyr+ groups increases in relation to the number of Phe groups.^{16,17}

3.2. Immersion Depth and Orientation of the Photosensitizers.

The sequence of events involved in the process of

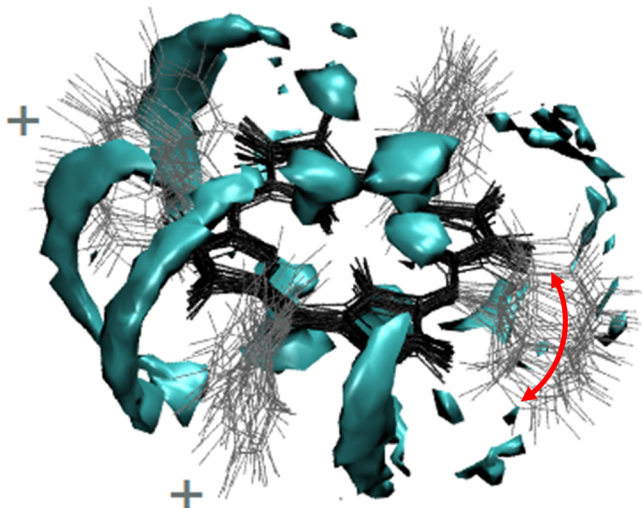


Figure 2. Equilibrated structure of P2c in aqueous solution. The central porphyrin ring (black) and all substituents (gray) are represented by lines, with the charged groups identified by the “+” sign. Individual simulation snapshots were superimposed at intervals of 4 ns, with the porphyrin ring as reference. Out-of-plane distortions of the substituents are indicated by the red arrow. The three-dimensional distribution of hydration water is represented by the blue isosurfaces, which enclose regions where the local water density is at least ca. 1.8 times higher than in the bulk.

Table 1. Experimental Properties from the Literature for Different Photosensitizers^{16,17}

compound	$\log P_{BW}^a$	k_H (au) ^{b,d}	C (%) ^{c,d}
P2c	0.63	3.73	50
P2t	0.79	0.86	25
P3	-0.56	0.38	10
P4	-1.97	0.06	10

^a*n*-Butanol/water partition coefficients in logarithmic scale. ^bHemolysis rate constants in arbitrary units. ^cApproximate fraction of the total amount of photosensitizers that effectively binds to the membrane. The total concentration was the same in all cases. ^dExperimental values obtained for photosensitizers with *N*-methyl-3-pyridinium substituents, similar to the *N*-methyl-4-pyridinium groups considered in simulations.

drug–membrane binding is shown in Figure 3 for the photosensitizer P2c (information for the other compounds is supplied in Figure S2, Supporting Information). All photosensitizers started at the aqueous phase and reached the membrane surface within the first 2 ns, driven by favorable drug–membrane electrostatic interactions. At 2 ns, the compound P2c was oriented with the Mpyr+ groups at the membrane surface and the Phe groups pointing toward the aqueous phase. In the sequence, it adsorbed at the membrane with its porphyrin ring parallel to the surface. Both Phe substituents were still significantly hydrated at this stage. At ca. 100 ns, the Phe substituents abruptly lost hydration and entered the membrane, while the partially hydrated Mpyr+ substituents remained close to the phosphate headgroups. Typically, photosensitizers needed up to ca. 200 ns to reach their equilibrium position and orientation at the lipid bilayer. The compound P3 was the only exception, as it took 300 ns to equilibrate. The lateral diffusion of the photosensitizers at the membrane surface was found to be negligible during the 100 ns of average data acquisition (Figure S3, Supporting Information).

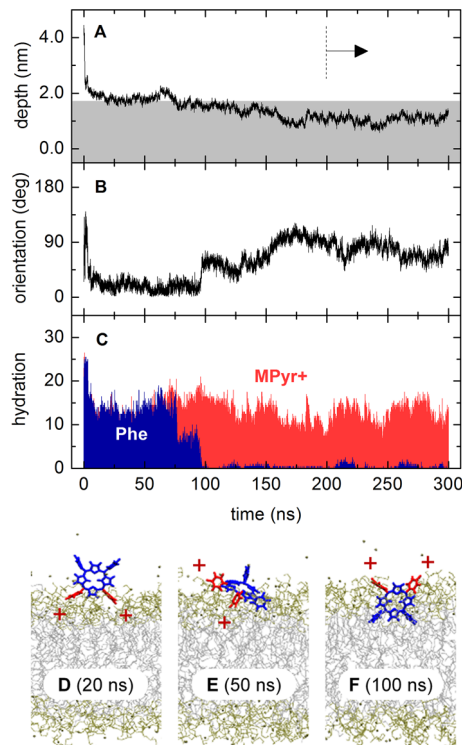


Figure 3. Temporal evolution of the drug–membrane binding process for P2c. (A) Immersion depth, as defined by the distance between the centers of mass of the photosensitizer and the bilayer. The shaded area corresponds to the region below the lipid phosphate groups, and the arrow indicates the starting point for the computation of averages. (B) Orientation of the photosensitizer, as defined by the angle between the porphyrin plane normal and the *z* axis. (C) Hydration of the substituent groups, as given by the number of solvent molecules within 6 Å of a reference atom (either the N atom at Mpyr+ or the corresponding C atom at Phe). (D–F) Simulation snapshots showing the lipid acyl chains (gray), the lipid headgroups plus counterions (brown), and the central porphyrin ring with the Phe (blue) and Mpyr+ (red, with the “+” sign) substituents.

tion). We found no significant change of the ordering of the lipid chains upon drug–membrane binding (Figure S4, Supporting Information). From all photosensitizers, P2c reached the largest immersion depth in the membrane. For comparison, we performed an additional simulation at physiologic ionic strength and did not find any significant change of the immersion depth and the orientation of P2c, despite the fact that a longer equilibration time was required (Figure S5, Supporting Information).

Figure 4 presents the average values of the equilibrium positions and orientations of the different photosensitizers at the membrane–water interface. It shows that the penetration depth toward the membrane interior was positively correlated with the degree of hydrophobicity in the case of the compounds P4, P3, and P2c. Surprisingly, the compound P2t strongly deviated from this trend. Its degree of hydrophobicity is similar to that of P2c, as inferred from the experimental values of *n*-butanol/water partition coefficients in Table 1. However, the immersion depth of P2t in the membrane was significantly smaller and comparable to that of the highly hydrophilic P4. This result points out that *n*-butanol/water (or alternatively *n*-octanol/water) partition coefficients have a limited predictive power for the partitioning of drugs between

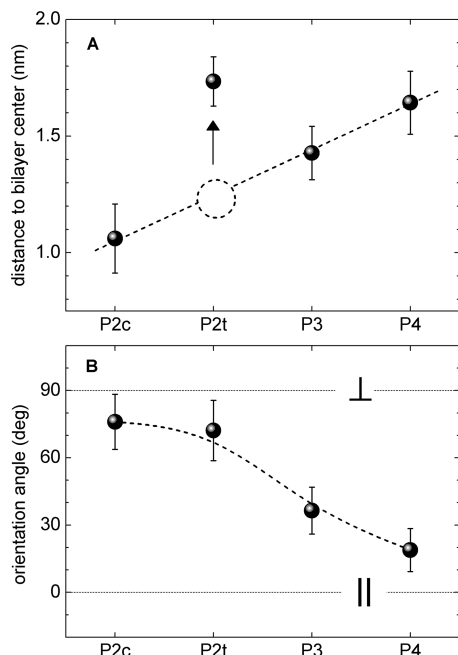


Figure 4. (A) Immersion depth and (B) orientation of different photosensitizers at the membrane–water interface, following the same definitions as in Figure 3. Equilibrium average values (black spheres with dashed eyeguides) are shown with the corresponding standard deviations (error bars). The dashed circle and the arrow highlight the deviating behavior of P2t. The limiting cases of the photosensitizer lying perfectly parallel (||) and perpendicular (⊥) to the bilayer surface are indicated by horizontal dashed lines.

a membrane and the aqueous medium, especially when dealing with chemical structures in which the amphiphilic character is directionally determined by a *cis-trans* isomerism.

The density profiles in Figure 5 give the spatial probability to find different molecules or functional groups along the bilayer normal. The membrane surfaces were heuristically defined at the peaks of the phosphate group distribution, since the water density dropped from its bulk value to zero within the region occupied by this group. Together, Figures 4 and 5 reveal that, after equilibrium was reached, the central porphyrin ring of P4 stayed almost flat at the bilayer surface. Adsorption was favored by the opposite charges beared by P4 and POPG, as indicated by the strong overlap between the distributions of the Mpyr⁺ groups and the Na⁺ membrane counterions. Similarly, in the case of P3, the central ring was almost parallel to the surface but slightly tilted so as to hide its only Phe substituent in the membrane interior. Differently, P2t and P2c were oriented perpendicular to the bilayer surface. In the case of the *trans* isomer, molecular geometry precluded concomitant access of both Phe rings to the membrane interior. One of the Phe groups reached the region slightly below the bilayer surface, while the other was kept almost fully hydrated and pointing toward the aqueous phase. The strongest amphiphilic character was exhibited by the *cis* isomer. In this compound, both Phe groups were deeply anchored in the membrane interior, while the two Mpyr⁺ groups remained partially hydrated at the membrane–water interface. The particular spatial arrangement assumed by each of the photosensitizers can be rationalized by saying that they tended to hide as many Phe groups as possible in the membrane interior, still preserving at least partial hydration of the Mpyr⁺ substituents and without disrupting their strong electrostatic interactions with phosphate head-

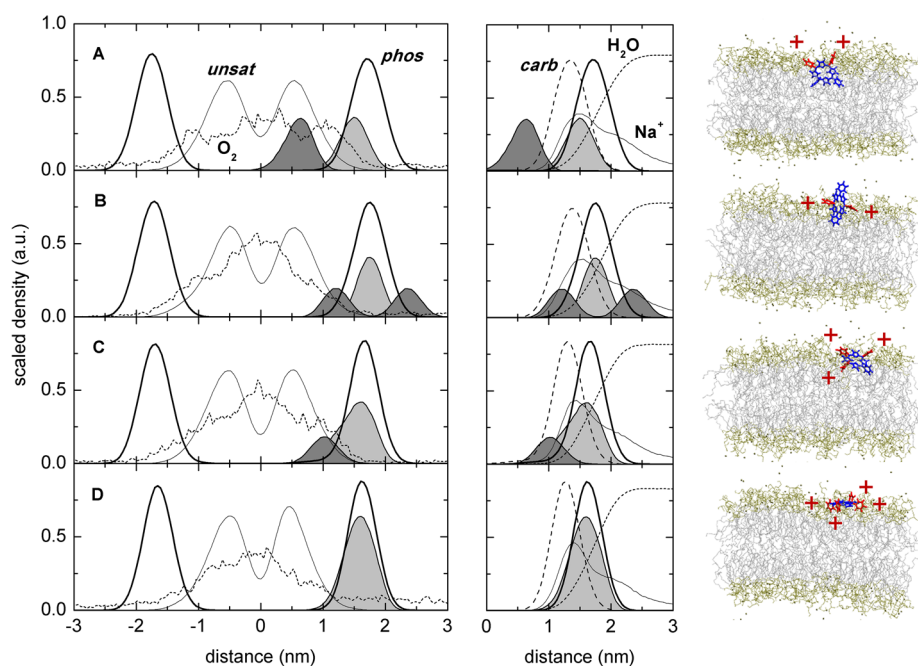


Figure 5. Density profiles along the *z* axis (left and central panels) for the photosensitizers (A) P2c, (B) P2t, (C) P3, and (D) P4. Shaded curves correspond to the MPyR⁺ (light gray) and Phe (dark gray) substituents of the photosensitizers and are compared to the distributions of lipid phosphate groups (phos, full lines), carbonylester groups (carb, dashed), hydrocarbon chain unsaturations (unsat, full), molecular oxygen (dotted), water (dotted), and Na⁺ ions (full). Density profiles were arbitrarily scaled for better visualization. The corresponding simulation snapshots (right column) show equilibrium configurations of the various photosensitizers, with MPyR⁺ and Phe groups represented in red (with the "+" sign) and blue, respectively.

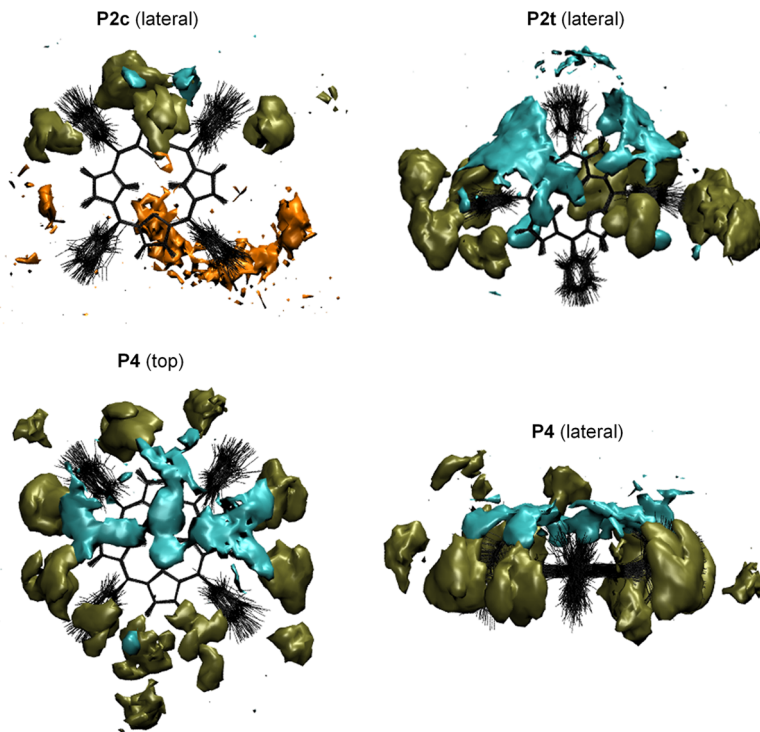


Figure 6. Top and lateral views of different photosensitzers (black) with respect to the membrane surface, showing the spatial distribution functions of water (blue) and lipid phosphate groups (brown). Photosensitzers are shown by a superposition of snapshots at 2 ns intervals. Isosurfaces correspond to a density of 0.018 and 0.005 atoms/nm³ for water and phosphate, respectively. The distribution of hydrocarbon chain unsaturations is shown only for P2c (orange, 0.006 atoms/nm³).

groups. Consequently, Mpyr+ groups were not able to penetrate into the membrane beyond the region of the carbonylester groups. These general trends are also supported by the three-dimensional SDFs depicted in Figure 6.

To evaluate the sensitivity of these results to the specific choice of the photosensitizer force field parameters, several independent sets of partial charges were taken from the literature and used to describe the photosensitzers.^{40,42–45} These charge sets were derived following different protocols (see Table S1, Supporting Information). However, Figures S6 and S7 (Supporting Information) demonstrate that the influence of the charge set over the immersion depth and orientation of P2c at the membrane–water interface was not sufficient to change the main qualitative features of the results presented in Figure 5. This indicates that fine details of the photosensitizer charge distribution are less relevant than basic structural characteristics such as the total charge and spatial distribution of charged and apolar substituents.

3.3. Photodynamic Efficiency at the Membrane–Water Interface. In PDT, type II reaction mechanisms rely upon energy transfer between a photosensitizer in its excited state and an oxygen molecule, resulting in the formation of ¹O₂. There is experimental evidence that points to the predominance of type II over type I reactions in lipid bilayers.⁶⁴ Membrane damage results from the tendency of ¹O₂ to add to hydrocarbon double bonds, forming hydroperoxides. The hydroperoxidation rate is higher in polyunsaturated as compared to monounsaturated lipids.⁸ Previous MD simulations indicate that the membrane permeability to water increases at the presence of lipid hydroperoxides and other oxidation products.^{65,66} The density profiles in Figure 5 predict an increased oxygen concentration in the membrane interior as compared with the aqueous phase, meaning that the double

bonds at the lipid hydrocarbon chains are very susceptible to peroxidation. In the process of photosensitization, the central porphyrin ring plays an important role because it is a π -conjugated system that acts as the chromophore. Therefore, the probability of ¹O₂ generation should increase with the ability of the chromophore to reach the oxygen-rich membrane interior. Figure 7 shows how the chromophores and the oxygen molecules are distributed along the bilayer normal. The probability of ¹O₂ generation via a type II mechanism (P_{II}) can be estimated, in the simplest way, in terms of the integral overlap between the density profiles of the chromophore (ρ_{chr}) and of molecular oxygen (ρ_{O_2}) along the z axis. This probability is expressed by

$$P_{II} \propto \int dz \rho_{chr}(z) \cdot \rho_{O_2}(z) \quad (2)$$

where the integral runs over the entire system length along the z axis. A direct correlation is assumed between photodynamic efficiency and the probability of ¹O₂ generation, as given by eq 2. Lipid peroxidation is not explicitly considered in the model because the reported lifetime of ¹O₂ in the lipid regions of membranes is found to vary from tens of nanoseconds⁶⁷ to tens of microseconds,⁷ indicating that it is at least comparable to the time scale accessed in MD simulations. These figures suggest that, in the case of an *in situ* photodynamic process, unsaturations do not need to be located at the immediacy of the ¹O₂ generation site to suffer peroxidation. The photodynamically generated ¹O₂ may have enough time to reach by diffusion even those lipids that are up to a few tens of nanometers away.

Figure 8 shows the relative photodynamic efficiencies of different photosensitzers, as determined by numerical integration of the density profiles according to eq 2. Before

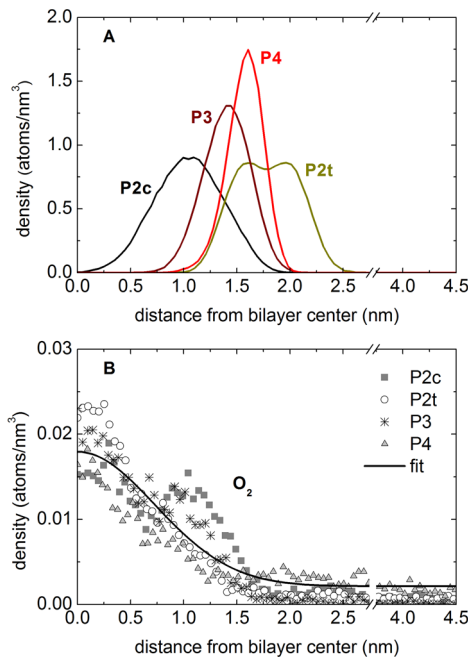


Figure 7. (A) Distributions of the chromophores of different photosensitizers along the z axis. (B) Oxygen distributions obtained from individual simulations (symbols) and the average distribution calculated by a Gaussian fit (full line). The baseline of the fit is related to the oxygen concentration in bulk water.

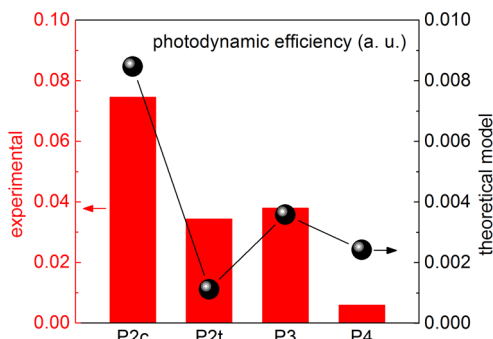


Figure 8. Comparison between the photodynamic efficiency predicted by simulations (black spheres) and experimental measurements of photodynamically induced hemolysis rates¹⁷ (red bars). All values are given in arbitrary units.

interpreting these data, it is convenient to inspect some of the experimental results reported by Engelmann et al.,¹⁷ which are summarized in Table 1. In the experimental work, the photodynamic efficiency was quantified in terms of cell lysis rates, which were measured *in vitro* using a series of cationic porphyrins to induce photodamage to erythrocytes. Analysis of the hemolysis rates in Table 1 shows an exceptionally high photodynamic efficiency for P2c when compared to the other photosensitizers. Part of this behavior can be attributed to the higher amount of adsorbed P2c molecules at the membrane–water interface. If the raw values of hemolysis rates are normalized by the amount of photosensitizer bound to the membrane, the relative efficiency of P2c decreases but is still at least twice as high as that of any other compound. This indicates that the photodynamic efficiency is also determined by details of the photosensitizer arrangement at the membrane–water interface. To remove the contribution of

concentration and compare the data to simulations, we divided the hemolysis rates by the effective surface concentration of photosensitizers. Figure 8 shows that the simulation results are in qualitative agreement with the concentration-normalized photodynamic efficiencies measured experimentally. In both cases, P2c is associated with the highest concentration-normalized photodynamic efficiency, reflecting its larger immersion depth into the membrane. In simulations, it was ca. 8 times more efficient than its isomer P2t. Besides that, simulations predicted a small increase in efficiency on going from P2t to P3. Experimentally, P2t is found to be slightly less efficient or at most comparable to P3. The largest differences between simulations and experiments are associated to the compound P4. Simulations predicted a ca. 4-fold decrease in photodynamic efficiency on going from P2c to P4, whereas this difference is ca. 12-fold in experiments. Nevertheless, we find these differences acceptable in view of the extreme simplicity of the theoretical model. Cell membranes in erythrocytes bear proteins and a significantly lower amount of anionic lipids as compared to the simulated POPG membranes. This might have contributed to an overestimation of the drug–membrane binding affinity in simulations, especially in the case of the highly charged P4. In fact, there was even a slight decrease of ca. 2 Å in the membrane thickness for the system containing P4. The significant degree of hydration of P4 when compared to the other compounds also suggests that it may be more susceptible to quenching effects by the solvent, which would lead to a lower efficiency than predicted by eq 2.

The combined analysis of experiments and simulations indicates that the photodynamic efficiency is mainly determined by the number of adsorbed photosensitizers and their arrangement at the membrane–water interface. When only structural factors were considered, P2t departed from the behavior of the other photosensitizers and exhibited an exceptionally small immersion depth, as already demonstrated in Figure 4. In simulations, this trend was reflected on the small concentration-normalized efficiency of P2t. However, if structural issues are considered in combination with the differences in local concentration, an exceptionally high photodynamic efficiency is to be expected for P2c. It results from the large immersion depth of P2c, associated with its exceptionally high affinity for the membrane. Figure S8 (Supporting Information) is supplied to illustrate the previous conclusions. These results give further theoretical evidence and a molecular explanation for the larger efficiency of amphiphilic photosensitizers as compared with nonamphiphilic ones.^{14–17} Experimentally, this effect has been known for a long time. However, there are also a few experimental observations that do not follow this general trend: zinc porphyrins are more hydrophilic than their free-base analogues, but the presence of the metal leads to a stronger binding affinity to membranes;^{68,69} an inverse correlation was found between liposomal uptake and *n*-octanol/water partition coefficients of very hydrophobic porphyrin photosensitizers.⁷⁰ Besides that, the presence of additives is known to affect the immersion depth of photosensitizers in liposomes,⁷¹ as is the case with poly(ethylene glycol) used for steric stabilization of the liposomes.⁷² All these effects are likely to involve specific interactions between the photosensitizers and the phospholipids. The investigation of the molecular mechanisms involved in these interactions will be a future extension of this work.

At this point, it is instructive to discuss a few assumptions and limitations of the theoretical model proposed here. In eq 2,

the probability of a close contact between an oxygen molecule and a chromophore is estimated using laterally averaged oxygen concentrations at different positions along the z axis. Quantification of the local oxygen concentration at the immediacy of the chromophore is a difficult task, given the fact that only a single oxygen molecule was present in each system. Due to large spatial fluctuations, it is also not possible to say whether the oxygen distribution is affected by the binding of the photosensitizers to the membrane. Another limitation of eq 2 is that it assumes that the probability of energy transfer between chromophores and oxygen depends only on the oxygen concentration. However, differences in polarity and hydration across the membrane could also play a significant role. In a previous simulation work, it was shown that the lateral diffusivity of oxygen is higher close to the bilayer center as compared to the lipid headgroup regions or the aqueous phase.¹⁸ We speculate that such an effect could contribute to a further raise in the efficiency of P2c with respect to the other photosensitizers.

In average, simulations predicted that the oxygen concentration is ca. 12 times higher in the membrane interior. Differently, experimental evidence suggests only an ca. 3–4-fold increase in concentration with respect to the aqueous phase.¹⁹ On the basis of the experimentally measured solubilities of oxygen in water and olive oil,⁵³ simulations were found to underestimate the affinity of oxygen for the aqueous phase. In view of the large spatial fluctuations of the oxygen distributions, these differences are acceptable and do not change the main qualitative results of the theoretical model. As shown in Figure 7, we were able to calculate an average oxygen distribution by fitting a Gaussian function to all four oxygen density profiles simultaneously. The baseline of the fit corresponds to the oxygen concentration in bulk water and was adjusted to be ca. 5 times lower than the average concentration inside the membrane. While simulations predicted an oxygen concentration of ca. 24 mg/L in the aqueous phase (standard deviation of 19 mg/L), a value of 57 mg/L was considered in the Gaussian fit, which is more compatible with experimental measurements of oxygen partition. We recall that these solubilities need to be rescaled to be compared to the oxygen solubility at ambient or physiological conditions since the presence of a single molecule in a simulation box already exceeds the experimental oxygen solubility at a partial pressure of 0.2 atm. In any case, the small difference between simulations and the Gaussian fit is hardly recognizable in the scale of Figure 7. When the Gaussian fit was taken as the oxygen distribution for all systems (see Figure S9, Supporting Information), the results were qualitatively very similar to those depicted in Figure 8. The main features were preserved, including the slightly higher efficiency of P3 as compared to P2t.

The proposed model was also based on the assumption that the distribution of the photosensitizer throughout the membrane is the same in both its fundamental and excited states. Recently, Nitschke et al.⁷³ demonstrated that the electronic state of the fluorescent probe PRODAN has a significant impact on its immersion depth in a lipid bilayer. It should be noted, however, that PRODAN is neutral with respect to its total charge. Differently, *meso*-(*N*-methyl-4-pyridinium)phenylporphyrins have integer values of the total charge. As demonstrated by the force field sensitivity test (see Figures S7 and S9, Supporting Information), details of the partial charge distribution within the compound P2c did not

change significantly the main qualitative results of the simulations. Although all charge sets used were aimed at a description of the fundamental state, we argue that the same principle of small sensitivity might apply when comparing the fundamental and the excited states of the photosensitizers. Structural characteristics such as the total charge of the photosensitizer and the spatial arrangement of charged and apolar substituents appeared to be the most influential for the immersion depth and orientation of these molecules. For a number of reasons, it is very likely that these basic features are preserved in the experimentally meaningful excited states. First, photoisomerization of the substituents is not possible, meaning that the chemical structures are preserved. Second, the high torsional energy barriers and the tilt angle of ca. 60° between the aromatic substituents and the porphyrin ring may prevent significant charge redistribution between the Mpyr+ group and the rest of the molecule.

Another important assumption of our model was that all photosensitizers had the same intrinsic $^1\text{O}_2$ generation efficiency. There is experimental evidence that different porphyrins bearing Mpyr+ and Phe groups have the same $^1\text{O}_2$ generation efficiency in air-saturated D_2O solution, provided that aggregation is prevented.¹⁷ There are, however, no direct measurements of the *in situ* intrinsic photodynamic efficiency of these photosensitizers when bound to lipid bilayers. To address this issue, classical MD simulations have a limited capability due to the absence of information about the electronic degrees of freedom. However, MD simulations can shed light onto aspects of the molecular structure that may have an influence over electronic processes. For instance, it has been suggested that intracellular adsorption of certain photosensitizers could cause rigidity of their structure, reducing rotational energy losses by the excited states and consequently improving photodynamic efficiency.³ We found, however, no indications of a significant change in the frequency of rotational transitions of the substituents in P2c after binding to the membrane (Figures S10, Supporting Information). An influence of membrane binding on the rigidity of the photosensitizer was evidenced only for P2t. The almost perpendicular, slightly tilted orientation of P2t with respect to the membrane surface caused the aromatic ring of MPyr+ substituents to be parallel with respect to the surface. The reduced rotational mobility of these groups probably resulted from the more effective interactions with the phospholipid headgroups.

For some of the photosensitizers, out-of-plane distortions of the substituents were found to be affected by the membrane. Four different conformer types were defined based on the out-of-plane distortions of the substituents with respect to the central porphyrin ring. They were named as “deck” (+, +, −, −), “chair” (+, +, +, −), “saddle” (+, −, +, −), and “dome” (+, +, +, +), where the signs in parentheses indicate out-of-plane distortions in opposing directions, as given by the dihedral angle between a substituent and a neighboring pyrrole ring. As shown in Figure 9, the chair conformation was the most prevalent in aqueous solution, corresponding to ca. 50% of all conformations. It was followed, in this same order, by deck, saddle, and dome, independent of the exact chemical structure of the photosensitizer. The binding of P2c to the membrane did not significantly change the distribution of conformers. However, in all other cases, the population of deck conformers almost doubled at the expense of the others, reaching the same importance as the chair conformation. These results may serve

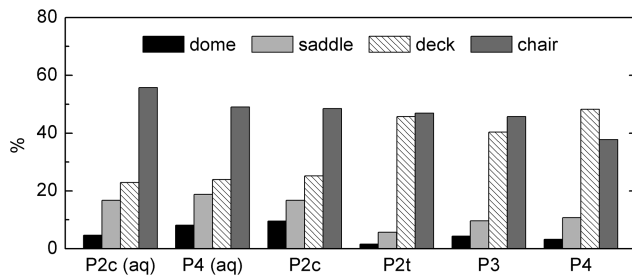


Figure 9. Conformer populations for various photosensitizers at the membrane–water interface and in aqueous solution (aq.).

as a starting point for electronic structure calculations to obtain clues about the *in situ* intrinsic photodynamic efficiency of different photosensitizers.

4. CONCLUSIONS

Molecular dynamics simulations were employed to provide a molecular view of the interactions between model lipid bilayers and cationic *meso*-(*N*-methyl-4-pyridinium)phenylporphyrin photosensitizers with different degrees of hydrophobicity (see Figure 1 for the chemical structures and nomenclature). We found that the immersion depth and the orientation of the photosensitizers depended on the relative number and spatial distribution of charged Mpyr⁺ groups and apolar Phe groups attached to the central porphyrin ring. In the case of compounds P2c and P2t, isomerism played a central role. Although these compounds have similar *n*-butanol/water partition coefficients, simulations predicted a much larger immersion depth for the *cis* compound. In the case of the *trans* isomer, molecular geometry precluded concomitant access of both Phe rings to the membrane interior. Our results explained at the molecular level why *n*-butanol/water (or alternatively *n*-octanol/water) partition coefficients have limitations in predicting drug–membrane interactions, especially when the amphiphilic character of a drug is determined by a *cis*–*trans* isomerism. We found that the accessibility of the photosensitizers to the hydrophobic and oxygen-rich membrane interior was correlated with experimental measurements of photodynamic efficiency. Results indicate that the *in situ* photodynamic efficiency depends on structural factors such as the position and orientation of the photosensitizers at the membrane–water interface, with amphiphilic photosensitizers exhibiting the largest efficiency. In terms of advances for PDT, the present work exemplifies how simulations can be used as a tool to propose improved structure–property relationships for photosensitizers. Experimentally, it has been known for a long time that amphiphilic photosensitizers perform better than nonamphiphilic ones. However, there are also a few experimental observations that do not follow this general trend. Consequently, it is necessary to develop theoretical tools that are able to consider specific molecular interactions of the photosensitizers with membranes. We believe that this work is an important step in this direction, and we hope that it will help us and others to understand in more detail the structure–activity relationships that drive the PDT efficiency.

ASSOCIATED CONTENT

Supporting Information

Force field parameters for the photosensitizers (Figure S1). Temporal evolution of the drug–membrane binding process for all photosensitizers (Figure S2). Lateral displacement of the

photosensitizers at the membrane surface (Figure S3). Lipid chain order parameters (Figure S4). Influence of the ionic strength in the drug–membrane binding (Figure S5). Force field sensitivity test (Table S1 and Figures S6, S7, and S9). Influence of structure and surface concentration (Figure S8). Rotation of the substituents (Figure S10). This material is available free of charge via the Internet at <http://pubs.acs.org>.

AUTHOR INFORMATION

Corresponding Author

*Phone: +55 11 49960173. E-mail: rodrigo.cordeiro@ufabc.edu.br.

Notes

The authors declare no competing financial interest.

ACKNOWLEDGMENTS

We acknowledge Fernanda Bettanin, Elierge Costa, Paula H. Mello, Mauricio D. C. Neto, and Thereza A. Soares for fruitful discussions. For the computational resources and technical support, we thank the scientific computing section of Universidade Federal do ABC. We also thank the National Council for Scientific and Technological Development (CNPq) and the São Paulo Research Foundation (FAPESP) for financial support.

REFERENCES

- Brown, S. B.; Brown, E. A.; Walker, I. *Lancet Oncol.* **2004**, *5*, 497–508.
- George, S.; Hamblin, M. R.; Kishen, A. *Photochem. Photobiol. Sci.* **2009**, *8*, 788–795.
- Wainwright, M. J. *Antimicrob. Chemother.* **1998**, *42*, 13–28.
- Hamblin, M. R.; Hasan, T. *Photochem. Photobiol. Sci.* **2004**, *3*, 436–450.
- Baptista, M. S.; Wainwright, M. *Braz. J. Med. Biol. Res.* **2011**, *44*, 1–10.
- Bristow, C. A.; Hudson, R.; Paget, T. A.; Boyle, R. W. *Photodiagn. Photodyn. Ther.* **2006**, *3*, 162–167.
- Ochsner, M. J. *Photochem. Photobiol. B: Biol.* **1997**, *39*, 1–18.
- Min, D. B.; Boff, J. M. *Compr. Rev. Food Sci. Food Saf.* **2002**, *1*, 58–72.
- Allison, R. R.; Sibata, C. H. *Photodiagn. Photodyn. Ther.* **2010**, *7*, 61–75.
- O'Connor, A. E.; Gallagher, W. M.; Byrne, A. T. *Photochem. Photobiol.* **2009**, *85*, 1053–1074.
- Ethirajan, M.; Chen, Y.; Joshi, P.; Pandey, R. K. *Chem. Soc. Rev.* **2011**, *40*, 340–362.
- Kępczyński, M.; Pandian, R. P.; Smith, K. M.; Ehrenberg, B. *Photochem. Photobiol.* **2002**, *76*, 127–134.
- Lavi, A.; Weitman, H.; Holmes, R. T.; Smith, K. M.; Ehrenberg, B. *Biophys. J.* **2002**, *82*, 2101–2110.
- Sholto, A.; Ehrenberg, B. *Photochem. Photobiol. Sci.* **2008**, *7*, 344–351.
- Caminos, D. A.; Spesia, M. B.; Pons, P.; Durantini, E. N. *Photochem. Photobiol. Sci.* **2008**, *7*, 1071–1078.
- Engelmann, F. M.; Rocha, S. V. O.; Toma, H. E.; Araki, K.; Baptista, M. S. *Int. J. Pharm.* **2007**, *329*, 12–18.
- Engelmann, F. M.; Mayer, I.; Gabrielli, D. S.; Toma, H. E.; Kowaltowski, A. J.; Araki, K.; Baptista, M. S. *J. Bioenerg. Biomembr.* **2007**, *39*, 175–185.
- Al-Abdul-Wahid, M. S.; Yu, C. H.; Batruch, I.; Evanics, F.; Pomès, R.; Prosser, R. S. *Biochemistry* **2006**, *45*, 10719–10728.
- Subczynski, W. K.; Hyde, J. S. *Biophys. J.* **1983**, *41*, 283–286.
- Stępniewski, M.; Kępczyński, M.; Jamróz, D.; Nowakowska, M.; Rissanen, S.; Vattulainen, I.; Róg, T. *J. Phys. Chem. B* **2012**, *116*, 4889–4897.

- (21) Casares, J. J. G.; Camacho, L.; Martín-Romero, M. T.; Cascales, J. J. L. *ChemPhysChem* **2010**, *11*, 2241–2247.
- (22) Eriksson, E. S. E.; Eriksson, L. A. *J. Chem. Theory Comput.* **2011**, *7*, 560–574.
- (23) Eriksson, E. S. E.; dos Santos, D. J. V. A.; Guedes, R. C.; Eriksson, L. A. *J. Chem. Theory Comput.* **2009**, *5*, 3139–3149.
- (24) Erdtman, E.; dos Santos, D. J. V. A.; Löfgren, L.; Eriksson, L. A. *Chem. Phys. Lett.* **2008**, *463*, 178–182.
- (25) Erdtman, E.; dos Santos, D. J. V. A.; Löfgren, L.; Eriksson, L. A. *Chem. Phys. Lett.* **2009**, *470*, 369–369.
- (26) Dowhan, W. *Annu. Rev. Biochem.* **1997**, *66*, 199–232.
- (27) Nishi, H.; Komatsuzawa, H.; Fujiwara, T.; McCallum, N.; Sugai, M. *Antimicrob. Agents Chemother.* **2004**, *48*, 4800–4807.
- (28) Hoch, F. L. *Biochim. Biophys. Acta* **1992**, *1113*, 71–133.
- (29) Rög, T.; Martinez-Seara, H.; Munck, N.; Orešić, M.; Karttunen, M.; Vattulainen, I. *J. Phys. Chem. B* **2009**, *113*, 3413–3422.
- (30) Schwarz, H. P.; Dahlke, M. B.; Dreisbach, L. *Clin. Chem.* **1977**, *23*, 1548–1550.
- (31) Virtanen, J. A.; Cheng, K. H.; Somerharju, P. *Proc. Natl. Acad. Sci. U.S.A.* **1998**, *95*, 4964–4969.
- (32) Allen, M. P.; Tildesley, D. J. *Computer Simulation of Liquids*; Clarendon Press: Oxford, 2009.
- (33) Frenkel, D.; Smit, B. *Understanding Molecular Simulation: From Algorithms to Applications*; Academic Press: San Diego, 2001.
- (34) Kukol, A. *J. Chem. Theory Comput.* **2009**, *5*, 615–626.
- (35) Oostenbrink, C.; Villa, A.; Mark, A. E.; van Gunsteren, W. F. *J. Comput. Chem.* **2004**, *25*, 1656–1676.
- (36) Berendsen, H. J. C.; Postma, J. P. M.; van Gunsteren, W. F.; Hermans, J. *Interaction Models for Water in Relation to Protein Hydration*; D. Reidel Publishing Company: Dordrecht, 1981; pp 331–342.
- (37) Fischer, J.; Lago, S. *J. Chem. Phys.* **1983**, *78*, 5750–5758.
- (38) Kučerka, N.; Holland, B. W.; Gray, C. G.; Tomberli, B.; Katsaras, J. *J. Phys. Chem. B* **2012**, *116*, 232–239.
- (39) Piggot, T. J.; Holdbrook, D. A.; Khalid, S. *J. Phys. Chem. B* **2011**, *115*, 13381–13388.
- (40) Barone, V.; Casarin, M.; Forrer, D.; Monti, S.; Prampolini, G. *J. Phys. Chem. C* **2011**, *115*, 18434–18444.
- (41) Karachevtsev, V. A.; Zarudnev, E. S.; Stepanian, S. G.; Glamazda, A. Y.; Karachevtsev, M. V.; Adamowicz, L. *J. Phys. Chem. C* **2010**, *114*, 16215–16222.
- (42) Guliaev, A. B.; Leontis, N. B. *Biochemistry* **1999**, *38*, 15425–15437.
- (43) Paulo, P. M. R.; Lopes, J. N. C.; Costa, S. M. B. *J. Phys. Chem. B* **2008**, *112*, 14779–14792.
- (44) Sambasivarao, S. V.; Acevedo, O. *J. Chem. Theory Comput.* **2009**, *5*, 1038–1050.
- (45) Jorgensen, W. L.; Maxwell, D. S.; Tirado-Rives, J. *J. Am. Chem. Soc.* **1996**, *118*, 11225–11236.
- (46) Hess, B.; Kutzner, C.; van der Spoel, D.; Lindahl, E. *J. Chem. Theory Comput.* **2008**, *4*, 435–447.
- (47) van Der Spoel, D.; Lindahl, E.; Hess, B.; Groenhof, G.; Mark, A. E.; Berendsen, H. J. C. *J. Comput. Chem.* **2005**, *26*, 1701–1718.
- (48) Darden, T.; York, D.; Pedersen, L. *J. Chem. Phys.* **1993**, *98*, 10089–10092.
- (49) Essmann, U.; Perera, L.; Berkowitz, M. L.; Darden, T.; Lee, H.; Pedersen, L. G. *J. Chem. Phys.* **1995**, *103*, 8577–8593.
- (50) Hess, B.; Bekker, H.; Berendsen, H. J. C.; Fraaije, J. G. E. M. *J. Comput. Chem.* **1997**, *18*, 1463–1472.
- (51) Hess, B. *J. Chem. Theory Comput.* **2008**, *4*, 116–122.
- (52) Miyamoto, S.; Kollman, P. A. *J. Comput. Chem.* **1992**, *13*, 952–962.
- (53) Battino, R.; Rettich, T. R.; Tominaga, T. *J. Phys. Chem. Ref. Data* **1983**, *12*, 163–178.
- (54) Wiedmann, T.; Salmon, A.; Wong, V. *Biochim. Biophys. Acta, Lipids Lipid Metab.* **1993**, *1167*, 114–120.
- (55) Nosé, S. *Mol. Phys.* **1984**, *52*, 255–268.
- (56) Hoover, W. G. *Phys. Rev. A* **1985**, *31*, 1695–1697.
- (57) Parrinello, M.; Rahman, A. *J. Appl. Phys.* **1981**, *52*, 7182–7190.
- (58) Nosé, S.; Klein, M. *Mol. Phys.* **1983**, *50*, 1055–1076.
- (59) Humphrey, W.; Dalke, A.; Schulter, K. *J. Mol. Graphics* **1996**, *14*, 33–38.
- (60) Poger, D.; van Gunsteren, W. F.; Mark, A. E. *J. Comput. Chem.* **2010**, *31*, 1117–1125.
- (61) Guizado, T. R. C.; Louro, S. R. W.; Anteneodo, C. *J. Chem. Phys.* **2011**, *134*, 055103.
- (62) Guizado, T. R. C.; Louro, S. R. W.; Pascutti, P. G.; Anteneodo, C. *Int. J. Quantum Chem.* **2010**, *110*, 2094–2100.
- (63) Guizado, T. C.; Pita, S. R.; Louro, S. R. W.; Pascutti, P. G. *Int. J. Quantum Chem.* **2008**, *108*, 2603–2607.
- (64) Girotti, A. W. *J. Photochem. Photobiol. B: Biol.* **2001**, *63*, 103–113.
- (65) Wong-ekkabut, J.; Xu, Z.; Triampo, W.; Tang, I. M.; Tielemans, D. P.; Monticelli, L. *Biophys. J.* **2007**, *93*, 4225–4236.
- (66) Lis, M.; Wizert, A.; Przybylo, M.; Langner, M.; Swiatek, J.; Jungwirth, P.; Cwiklik, L. *Phys. Chem. Chem. Phys.* **2011**, *13*, 17555–17563.
- (67) Kanofsky, J. R. *Photochem. Photobiol.* **1991**, *53*, 93–99.
- (68) Pavani, C.; Iamamoto, Y.; Baptista, M. S. *Photochem. Photobiol.* **2012**, *88*, 774–781.
- (69) Pavani, C.; Uchoa, A. F.; Oliveira, C. S.; Iamamoto, Y.; Baptista, M. S. *Photochem. Photobiol. Sci.* **2009**, *8*, 233–240.
- (70) Ben-Dror, S.; Bronshtein, I.; Wiehe, A.; Röder, B.; Senge, M. O.; Ehrenberg, B. *Photochem. Photobiol.* **2006**, *82*, 695–701.
- (71) Kępczyński, M.; Nawalany, K.; Kumorek, M.; Kobierska, A.; Jachimska, B.; Nowakowska, M. *Chem. Phys. Lipids* **2008**, *155*, 7–15.
- (72) Cordeiro, R. M.; Zschunke, F.; Müller-Plathe, F. *Macromolecules* **2010**, *43*, 1583–1591.
- (73) Nitschke, W. K.; Vequi-Suplicy, C. C.; Coutinho, K.; Stassen, H. *J. Phys. Chem. B* **2012**, *116*, 2713–2721.